A gold nanoparticle-enhanced methylene blue electrochemical sensor for detecting waterborne anionic surfactants and PFAS

Federica Simonetti [a,*], Riccardo Buccini[b], Valentina Migliorati[c], Marco Mancini[d], Daniele Caterino[e], Valentina Gioia[d], Marco Agostini[a], Franco Mazzei[a], Alessandro Ciccola[b], Gabriele Favero[b], Rosaceleste Zumpano[a]

[a] *Department of Chemistry and Drug Technologies, Sapienza University of Rome, P.le Aldo Moro 5, 00185, Rome, Italy*

[b] *Department of Environmental Biology, Sapienza University of Rome, P.le Aldo Moro 5, 00185, Rome, Italy*

[c] *Department of Chemistry, Sapienza University of Rome, P.le Aldo Moro 5, 00185, Rome, Italy*

[d] *Department of Organic Micropollutants, Acea Infrastructure, Via Vitorchiano 165, 00191, Rome, Italy*

[e] *Department of Science and Engineering of Matter, Environment and Urban Planning, Marche Polytechnic University, Via Brecce Bianche 12, 60131, Ancona, Italy*

Abstract

Anionic surfactants (ASs) represent a class of contaminants persistently released into aquatic environments, with anionic fluorinated surfactants emerging as a significant concern due to their potential to infiltrate potable water and pose a threat to human health. Therefore, the development of novel tools for their early detection is crucial. In this study, the methylene blue (MB) redox probe, previously known for its selectivity toward ASs, was electropolymerized onto the surface of carbon nanotubes -modified graphite screen-printed electrodes. The electroanalytical ability of the platform was tested by cyclic (CV) and square-wave (SWV) voltammetries upon the addition of sodium dodecyl sulfate as model analyte, due to its ubiquitous presence in the environment. A comprehensive exploration of key factors, such as scan cycles, optimal instrumental parameters, and pH effect was undertaken, revealing a stable and controlled redox response. To further enhance the sensitivity and detection capabilities of the MB-based sensor, gold nanopar-

*Corresponding author

Email address: f.simonetti@staff.univpm.it (Federica Simonetti [a,*])

Preprint submitted to Elsevier *June 12, 2025*

ticles (AuNPs) were incorporated, forming MB@AuNPs-modified electrodes. This enhanced system demonstrated excellent linearity (0.051 ng/mL and 550 ng/mL), high reproducibility, and improved detection limits (8.5 pg/mL and 0.23 ng/mL), attributed to the synergistic effect of MB and AuNPs in boosting the reduction current. The sensor was successfully applied to wastewater samples, benchmarked against the MBAS reference method, and further validated for the detection of two long-chain PFAS in drinking water. Supported by quantum mechanical calculations and optical studies, this proof-of-concept platform represents a sustainable approach for efficient water quality monitoring and management.

Keywords:
CEC, surfactants, PFAS, water monitoring, quality control, efficient management

---

1. Introduction

With global consumption steadily increasing and the market projected to reach USD 58.04 billion by 2028 (Muthaiyan Ahalliya et al. (2023); Arora et al. (2022)), surfactants are extensively used as active ingredients in a broad range of pharmaceuticals and consumer care products, as well as in household and industrial applications. Anionic and non-ionic surfactants account for the majority of production (Gomez et al. (2011); Nakama (2017)), with anionic types demonstrating intrinsic bioactivity by interacting with proteins and altering the permeability of cell membranes (Deep and Ahluwalia (2001); Iqbal et al. (2005); Prieto et al. (1993); Keller et al. (2006); Pereira et al. (2015); Tolls et al. (1994)). Their high degree of sorption across environmental compartments, solvent properties, toxicity, and foaming capacity make them harmful to ecosystems and public health, contributing to water quality degradation and climate change (Cserhti et al. (2002); Badmus et al. (2021)). Among the numerous surfactants discharged into the environment, fluorinated anionic surfactants stand out as a significant subgroup of perfluoroalkyl compounds (PFAS). Despite their chemical similarity to aliphatic anionic surfactants, these pollutants exhibit heightened resistance to biological degradation and prolonged environmental persistence due to the high energy of the C-F bond (536 kJ/mol) (Podder et al. (2021); Panieri et al. (2022); Kovalchuk et al. (2014); Simonetti et al. (2025b)). Perfluorooctanoic acid (PFOA) and perfluorooctanesulfonic acid (PFOS), the two

more common representatives of this class, have been detected in many water bodies (Kurwadkar et al. (2022); Möller et al. (2010); Wang et al. (2019); Kim and Kannan (2007)), which serve as their natural sinks, as well as in other environmental media such as biota and air (D'Ambro et al. (2020); Chen et al. (2023); Barber et al. (2007); Cara et al. (2022)). They have also been found in biological samples, including human serum, plasma and whole blood (Poothong et al. (2017)) and have been associated with several health conditions (Canova et al. (2020); Domingo and Nadal (2019); Fenton et al. (2021)). Due to the trace concentrations, most of the analyses are carried out using chromatographic separation methods coupled with mass spectrometry (HPLC-MS/MS) conducted in professional laboratories (Al Amin et al. (2020); Badmus et al. (2021); Mancini et al. (2023)). These analytical protocols could involve a preconcentration step that extends the analysis time and reduces the reproducibility and sensitivity of the method. Moreover, particularly for PFAS, the use of isotopically labeled internal standards, which are not always readily available, significantly increases the analysis costs and challenges the accurate and specific identification of less conventional and emerging PFAS (Podder et al. (2021)). Considering the limits of current analytical methods, the development of rapid and sensitive sensors represents a promising alternative (Menger et al. (2021); Simonetti et al. (2025c)). Electrochemical sensors stand out for their sensitivity, simplicity, efficiency, and portability, driving research into new approaches despite PFAS inertness (Simonetti et al. (2025a)). Strategies include molecular imprinted polymers (MIPs)-modified electrodes combined with nanoparticles (Lu et al. (2022a); Gao et al. (2023)) or fluoropolymers (Sahu et al. (2022)), the exploitation of surface activity-driven detection (Ranaweera et al. (2023); Khan et al. (2022)), and ion transfer across immiscible phases (Garada et al. (2014a)). However, current sensors remain primarily limited to the detection of PFOA and PFOS, while the extremely low target concentration limits demand exceptionally high sensitivity and selectivity, which they often fail to achieve (Lamichhane and Arrigan (2023)). To address these limitations, this study presents a novel two-step electrochemical sensing platform based on the selective interaction between methylene blue (MB) and anionic surfactants, extended to PFAS detection, by-passing extraction steps and enabling ppt-level detection. First, MB was electropolymerized onto carbon nanotube (CNT)-modified electrodes to create a redox-active surface, which was evaluated using sodium dodecyl sulfate (SDS) as a model compound. To further enhance sensitivity, the platform was subsequently integrated with gold nanoparti-

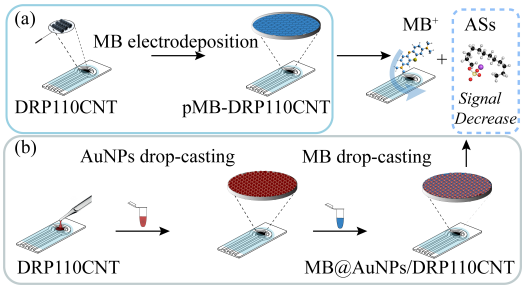

Figure 1: Virtual prototypes of (a) p−MB DRP110CNT and (b) MB@AuNPS/DRP110CNT platforms realized in Inventor CAD.

cles (AuNPs), which offer several advantages for improving electrochemical sensor performance (Polli et al. (2023)). Specifically, various studies have demonstrated their ability to enhance the opto-electronic properties of thiazine dyes, particularly with regard to UV-Vis absorption and electrochemical signals (Narband et al. (2009); Shan et al. (2021); Khan et al. (2012); Cheng et al. (2001)). The analytical performance of this second platform was thoroughly evaluated, considering key parameters such as linear detection range, reproducibility, sensitivity, and temporal stabilityall of which confirmed favorable sensing characteristics. Moreover, its robustness and high selectivity against interfering surfactants, including cationic and zwitterionic species, combined with its remarkable sensitivity in the ppt concentration range, underscore its potential for PFAS detection. In this regard, computational studies suggest that PFAS electrochemical sensing is facilitated by hydrophobic and polar interactions between the monomers and MB. Initial electrochemical tests conducted on one short-chain PFAS and two long-chain PFAS perfluorobutanoic acid (PFHBA), perfluorooctanesulfonic acid (PFOS) and perfluoroundecanoic acid (PFUnDA)revealed an even stronger response than that observed for hydrocarbon surfactants. These promising results present the future prospect of detecting these less biodegradable compounds, which, unlike hydrocarbon-based surfactants, can infiltrate drinking water systems, posing a threat to human health. This approach addresses the need for affordable, ready-to-use solutions that support safe and effective water management (Simonetti et al. (2025a)).

2. Outline

Common analytical methods for the determination of anionic surfactants in water are based on the use of MB, which selectively interacts with anionic surfactants to form ion-pairs that are soluble in organic solvents (Carroll et al. (1999); Wyrwas and Zgoła-Grześkowiak (2014); Shyichuk and Ziółkowska (2016); González-López et al. (2021); Ródenas-Torralba et al. (2005); Jurado et al. (2006); George and White (1999); Germani et al. (2021)). Recent developments in the state of the art have demonstrated that PFAS are also considered Methylene Blue Active Substances (MBAS) (Tang et al. (2025); Rehman et al. (2025); Fang et al. (2018); Lada et al. (2024)). This work presents the development of a two-step electrochemical platform for PFAS detection based on the methylene blue active substances (MBAS) principle, adapted into a solid-state configuration. The sensing strategy is structured as described in Fig. 1: a) as a proof of concept, MB was immobilized via electropolymerization onto multi-walled carbon nanotube (MWCNT)-modified screen-printed graphite electrodes. This approach eliminates the need for liquidliquid extraction and enables direct electrochemical interrogation of surfactantMB interactions. The system was initially tested with sodium dodecyl sulfate (SDS) to optimize experimental conditions such as scan cycles, pH, and instrumental parameters, ensuring signal stability and reproducibility. b) To enhance the sensors sensitivity and detection capability, gold nanoparticles (AuNPs) were introduced to form the MB@AuNPs modified electrode. The resulting platform was evaluated using both model surfactants and real water samples, and was then applied to the detection of one short-chain PFAS and two long-chain PFAS (e.g., PFHBA, PFOS, PFUnDA), confirming its ppt-level sensitivity and strong selectivity even in complex matrices.

3. Experimental

3.1. Chemicals and reagents

HAuCl_4 (99,99% MW 339.79 g/mol, d=1,637 g/ml a 25 C) and sodium citrate ($C_6H_5Na_3O_7 \cdot 2H_2O$, MW 294.10 g/mol, 99,99%) employed in the synthesis of gold nanoparticles were purchased from Merck-Sigma-Aldrich. Sodium dodecyl sulfate (SDS, $NaC_{12}H_{25}SO_4$, MW 288.38 g/mol), polyethylene glycol sorbitan monolaurate (TWEEN 20, $C_{58}H_{114}O_{26}$, 10% w/v aqueous), cetyltrimethylammonium bromide (CTAB, $C_{19}H_{42}BrN$, MW 364.45 g/mol), sodium laureth sulfate (SLES, $CH_3(CH_2)_{11}(OCH_2CH_2)NOSO_3Na$,

MW 288.38 g/mol), sodium tetraborate (BORAX, $Na_2B_4O_7$, MW 201.22 g/mol, 99,99%), benzyldimethylhexadecylammonium chloride (16-BAC, $CH_3(CH_2)15N(Cl)(CH_3)_2CH_2C_6H_5$, MW 396.06) and methylene blue (MB, $C_{16}H_{18}ClN_3S$, MW 319.85 g/mol) were also purchased from Merck-Sigma-Aldrich. Calcium chloride dihydrate ($CaCl_2 \cdot 2H_2O$, MW 147.01 g/mol), sodium chloride (NaCl, MW 94.47 g/mol), EDTA disodium salt ($C_{10}H_{14}N_2$ $Na_2O_8 \cdot 2H_2O$, MW 372.24 g/mol) were purchased from Carlo Erba. Sodium perfluooctansulfonate acid (PFOS, $C_8F_{17}SO_3H$, MW 500.13, 50 mg/L, MeOH) and sodium perfluoroundecanoic acid (PFUnDA, $CF_3(CF_2)_9CO_2H$, MW 564.09 g/mol, 50 mg/L, MeOH) solutions were purchased from Wellington Lab, while heptafluorobutyric acid (PFHBA, $C_4H_7F_7O_2$, MW 214.04 g/mol, 99,99%) and butyric acid ($C_4H_8O_2$, MW 88.11 g/mol, 99,99%) were purchased from Thermo Fisher Scientific. All materials used for PFAS analysis were purchased PFAS-free and tested before the usage.

3.2. Procedures

All measurements were performed at room temperature under magnetic stirring, using newly modified screen-printed electrodes as the working electrode, and silver/silver chloride and graphite as the reference and counter electrodes, respectively.

3.2.1. MB@AuNPs synthesis

AuNPs were synthesized using the Turkevich method (Turkevich et al. (1951)). For the functionalization with MB, 3.2 mL of AuNPs were combined with 600 μL of MB at a concentration of 20 μM. The solution was left under stirring for one hour and half. Once, nanoparticles exhibited approximately 20% lower absorbance and shifted towards violet (Fig. S3). The functionalized nanoparticles were then centrifuged three times at 12000 rpm for 10 minutes and used.

3.2.2. p−MB DRP110CNT and MB@AuNPS/DRP110CNT electrodes

The DRP110CNT screen printed electrodes were modified by electrodeposition of p-MB sweeping the potential between −0.356 to 1.244 V vs. Ag/AgCl in 0.25 mM MB solution (0.02 M borate buffer pH 9.14, supporting electrolyte 0.1 M KNO_3, sweep rate 50 mV mVs^{-1}) (Zumpano et al. (2020)). The modified electrode was then rinsed twice and immersed overnight in the 3 mL buffer solution to remove the excess (Fig. 1a). The MB@AuNPS/DRP110CNT was made by drop−casting a first layer of 5 μL

AuNPs onto the working electrode (WE) of DRP−110CNT SPE. Once adsorbed, a second layer of MB (10 μL, 40 μM) was deposited onto the WE and any unbound MB was subsequently removed (Fig. 1b).

3.2.3. Response measurements

Using square wave voltammetry (SWV), all response measurements were performed by incrementally adding SDS solutions (V= 10 μL) to PBS, with each measurement repeated seven times to ensure reproducibility.

3.2.4. Matrix effects, selectivity, and method validation

The matrix effect was evaluated as the difference between the current intensity of the standard in buffer (I_{buffer}) and the current intensity of the standard in the matrix (I_{matrix}) the cathodic peak potential (Epc) of -0.26, as:

$$\frac{I_{buffer} - I_{matrix}}{I_{buffer}} \cdot 100\% \tag{1}$$

The selectivity of the platform was evaluated by testing its response to anionic surfactant SLES, non-ionic surfactant TWEEN20, and cationic surfactants CTAB and BAC. The response was calculated as:

$$\frac{I_{surfactant}}{I_{std}} \cdot 100\% \tag{2}$$

where $I_{surfactant}$ is the signal of the tested surfactants and I_{std} , that of the standard. To further assess the platforms resistance to interference, its response was tested in a PBS solution containing SDS (25 ng/mL) and a range of potential interfering species. These included Na^+ and Ca^{2+} at two concentrations (0.1 M and 0.5 M), as well as EDTA, citrate, and borate (each at 0.1 M). The variation in signal response due to interference, evaluated over 7 replicates, was calculated using the formula:

$$\frac{(I_{std} - I_{std/int})}{I_{std}} \cdot 100\% \tag{3}$$

where $I_{std/int}$ is the signal of the standard in presence of interferences. For the validation step, municipal wastewater samples were diluted 1:100 in phosphate-buffered saline (PBS) and analyzed using square wave voltammetry (SWV) and the standard addition method. The results were compared with those obtained using the MBAS method (see Supporting Information for further details). To assess the methods suitability for PFAS analysis,

tap water samples were spiked with PFAS standard compounds. Recovery values (n=3) were compared with those obtained using an accredited UHPLC-MS/MS method described elsewhere (Mancini et al. (2023).

3.2.5. Data analysis and visualization

Data were analyzed and visualized using Python (version 3.7). Standard deviations are reported as error bars, and the number of replicates (n) is indicated for each measurement.

3.3. Instruments

All measurements were conducted in an electrochemical cell, where the saturated silver/silver chloride electrode and graphite electrode act as the reference and counter electrodes, respectively. Screen-printed graphite electrodes modified with multi-walled carbon nanotubes (DRP110CNT) were purchased from Metrohm and used as the working electrodes. Electrochemical measurements (CV, DPV, and SWV) were performed using a PalmSens potentiostat (Palmsens3). UV-Vis spectra were acquired over a wavelength range of 190 to 800 nm through T60U-Spectrometer UV-Vis spectrophotometer (PGinstrument Ltd). Raman spectroscopy (HORIBA LabRAM HR Evolution with LabSpec software) was used to analyze the surface of the WE. For comprehensive sample analysis, point measurements and mapping were performed at 9 points (15mWatt, λ=632.8 nm, 120 s/scan, scan =3). Scanning electron microscopy (SEM) measurements have been carried out with High-Resolution Field Emission Scanning Electron Microscopy (HR FESEM, Zeiss Auriga Microscopy). Validation measurements were carried out with a UHPLC-MS/MS system comprised a Thermo Scientific UHPLC UltiMate 3000 system fitted with a Thermo Scientific TSQ Altis triple quadrupole mass spectrometer equipped with a ESI ionization probe. UHPLC-MS/MS method details are reported elsewhere (Mancini et al. (2023)).

3.4. Quantum Mechanical Calculation Details

Quantum Mechanical (QM) calculations on three clusters, each composed of one methylene blue (MB) cation and one anion, namely dodecyl sulfate (DS), perfluorooctanesulfonate (PFOS), or perfluoroundecanesulfonate (PFUnDA), have been carried out by means of the Orca4.2.1 package (Neese (2012)), using the density functional theory. Full geometry optimization of the cluster and of the separate fragments were performed using the PBE functional (Perdew et al. (1996)). The energies have then been calculated

by using the hybrid B3LYP functional. The all-electron def2-SVP basis set has been employed to describe all of the atoms of the systems (Weigend and Ahlrichs (2005)). Solvent effects have been implicitly included in the calculations by using the CPCM solvation model with water as solvent (Barone and Cossi (1998)). Dispersion force corrections were included with the DFT-D3 method, together with the Becke-Johnson damping function (Grimme et al. (2011)). All optimized structures were further post-processed with Multiwfn 3.8 (Lu and Chen (2012)), and several quantum chemistry descriptors were also visualized with VMD 1.9.3 software (Humphrey et al. (1996)). The nature of intermolecular interactions was investigated using the Independent Gradient Model based on Hirshfeld partitioning (IGMH), implemented in the main function 20 (visual study of weak interaction) of Multiwfn, as described by Lu and Chen (2022). The IGMH can portray covalent and non-covalent interactions counterparts in two intra- and intermolecular regions expressed as follow:

$$\delta g = \delta g_{intra} + \delta g_{inter} \tag{4}$$

where δg_{intra} and δg_{inter} indicate intramolecular and intermolecular contributions to the gradient of electron density, respectively. This method was employed to calculate the three-dimensional real space function δg_{inter} and the color-filled maps of δg_{inter} was drawn via the VMD code in order to highlight the different interactions.

4. Results and discussion

4.1. Electropolymerization of MB, characterization, and optimization of the p-MB/DRP-110CNT

A thin layer of MB was electropolymerized onto the electroactive surface of a DRP-110 CNT screen-printed electrode, following a previously established protocol (Zumpano et al. (2020)) by using CV, with some modifications. Four characteristic peaks can be identified in the voltammograms (Fig. 2a) (Pfaffen et al. (2010)): a) the anodic peak at -0.2 V related to the monomer consumption, decreasing in current intensity during the reaction; b) the couple of anodic and cathodic peaks at 0.06 V and -0.12 V respectively, related to the polymer formation, progressively increasing in current intensity; c) the anodic peak at 1 V, presumably referred to the cationic radical formation during the reaction (Pfaffen et al. (2010)).

As emphasized in the literature (Yogeswaran and Chen (2008); Cheng et al. (2001)), Multi-Walled Carbon Nanotubes (MWCNTs) play a pivotal

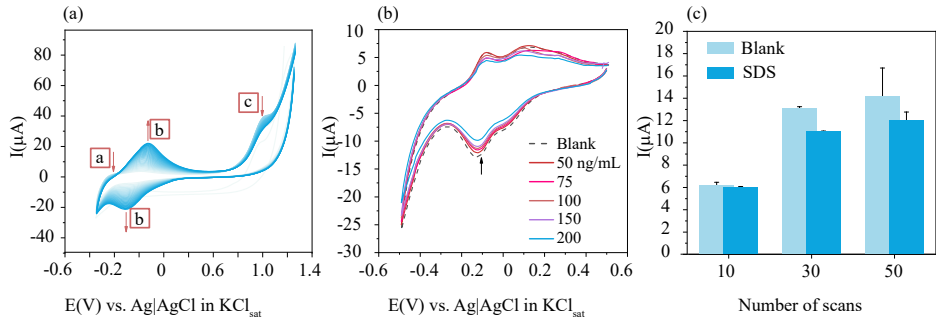

Figure 2: (a) Electrochemical polymerization of MB (0.25 mM) in a 0.02 mM borate buffer solution at pH 9.3, with a scan rate of 50 mV/s for 30 scans on a DRP110CNT electrode. (b) CV of p-MB/DRP110CNT in the presence of different concentrations of SDS (50 μg/L - 200μg/L, acetate buffer) and (c) electrode response at different number of scans. Error bars represent standard deviations (n=10).

role in the polymerization process, by enhancing both the electrode coverage degree and the electron transfer rate, while reducing the polymer degradation time. The electrode coverage degree after 30 scanning cycles was estimated from the polymer surface concentration (Γ). Γ was calculated from the charge associated with the electropolymerization process (Q), using the following expression (Braun et al. (2017)) (Eq. 5):

$$\Gamma = \frac{Q}{nFA} \tag{5}$$

where A is the geometric area of the electrode equal to 0.1256 cm^2, n is the number of electrons (n=2), F is the Faraday constant (96485.33 Cmol^{-1}), and Q is the charge involved in the electrochemical process (8.87 1.12 μC), estimated by integrating the oxidation peak related to the thirtieth cycle between -0.2 V and 0.5 V of p-MB. Based on these values, Γ is determined to be 3.66 10^{-10} mol/cm^2. In line with our previous findings (Zumpano et al. (2020)), the polymer thickness is 1.46 nm, calculated as $d = v$ x Γ where v is the molecular thickness of MB in the film, equal to 400 cm^3/mol (Marinho et al. (2012)). To evaluate the electrochemical capacity of the platform for SDS detection, several CVs were acquired in acetate buffer (pH=5) in a potential window ranging from +0.5 V to -0.5 V in a concentration range of 50 ng/mL to 200 ng/mL (Fig. 2b) . In the absence of surfactant, the electrochemical profile shows stable anodic and cathodic peaks at approximately -0.08 V and -0.17 V, respectively. Upon surfactant addition, the current

intensity decreases for both peaks, particularly the cathodic one. This reduction is probably due to ionic and hydrophobic interactions between the cationic dye MB and the anionic surfactant SDS, forming strong ion pairs insoluble in water (Junqueira et al. (2002); George and White (1999)). Considering the Lewis acid-base properties of MB and SDS, this interaction may involve the dye's amino group, stabilizing the ion pair (Taj Muhammad and Khan (2017)). SDS molecules adsorb onto the p-MB electrode, increasing the surface negative charge and forming an insulating layer that hinders charge transfer at the electrode, thereby affecting the electrochemical response (Cachet et al. (1993); Sen et al. (2016)).

4.2. Optimization of Electrochemical SDS Sensing

To optimize the platforms response, several parameters were examined. The number of polymerization cycles (10, 30, 50) was varied, showing that the electrochemical signal increased with more cycles, apparently reaching a plateau (Fig. 2c). In this regard, the stability of the polymer after 50 cycles decreased, as indicated by repeated 5-minute voltammograms (data not shown), despite keeping the electrode in buffer solution overnight. Considering the electrochemical response, realization time, and stability, 30 cycles were found to provide the best conditions, consistent with the findings of Braun et al. (2017). The redox behavior of p-MB, which is pH-dependent, was tested across a pH range of 5-9 (Fig. 3a-b). At acidic pH, p-MB exhibited quasi-reversible behavior, while alkaline pH led to reduced electrochemical activity, likely due to polymer degradation. After adding SDS, a decrease in current was observed, especially at pH 5-7, due to interactions between SDS and the electrode surface. Plotting E_{pc} as a function of pH (Fig. 3c) reveals a perfectly linear trend (E_{pc} = -0.050pH +0.05, R^2 =0.982 in the presence of SDS and E_{pc} = 0.049pH +0.07, R^2=0.995 in the absence of SDS). Considering the Nernst equation for pH (Eq. 6):

$$E = E^0 - \frac{2.303mRT}{nF}pH \tag{6}$$

From the slope of the line (50 mV/pH), it is possible to derive the ratio m/n (where m represents protons and n represents electrons), which is approximately 2/3. Therefore, in the process, 2 protons and 3 electrons are exchanged. Plotting the cathodic peak intensity at around -0.17 V as a function of pH in the presence and absence of SDS (Fig. 3d), it is possible to observe greatest differences in terms of current at pH values between 5 and

7. Since the sensor is intended for the analysis of water samples, pH was set to 7 in phosphate buffer. To characterize the redox process, several voltammograms were acquired by cyclically varying the potential at different scan rates (Fig. 4a). From the double log plot (Laviron (1979)) of the oxidation peak current as a function of scan rate (Fig. 4b), a linear trend ($R^2 = 0.994$) can be observed, indicating the dependence of the process on both the diffusion and the adsorption of the species to the electrode. As observed by Sun et al. (Sun et al. (2012)), the dual oxidation and reduction peaks could be attributed to the oxidation/reduction and doping/de-doping processes of p-MB. Using the Laviron equation (Laviron (1979)) (Eq. 7), it is possible to calculate the transfer coefficient and the electron transfer rate constant, respectively α and K_s:

$$E_{pc} = E^0 - \frac{RT}{(1-\alpha)nF} ln \frac{TK_s}{(1-\alpha)nF} - \frac{RT}{(1-\alpha)nF} lnv \tag{7}$$

From the Eq. 7, we obtain $\alpha = 0.274$ and $K_s = 0.186$ s^{-1} (for v > 150 mV/s). These values are lower than the standard values of the electrodes modified with CNT and p-MB, where $\alpha \sim 0.5$ and $K_s \sim 0.7$ s^{-1} (Sun et al. (2012)), thus confirming the possible degradation of the p-MB layer. The electron transfer coefficient α is less than 0.5: when the potential varies little with the scan rate, it indicates slow kinetics in which the analyte is strongly adsorbed on the electrode.

Consequently, since the kinetics are slower, in order to increase electron transfer and improve sensor sensitivity by reducing capacitive current, calibration was performed using Square Wave Voltammetry (SWV) measurements. Various accumulation (preconcentration) times were also evaluated to optimize the signal and further increase the sensitivity of the technique. Fig. S4 shows the impact of accumulation time on SWV measurement for SDS at a potential of 0.00 V. The peak current increased up to 150 s, after which no substantial change in peak current was observed. Consequently, an accumulation time of 150 s was selected for all subsequent measurements. The sensor was calibrated directly in aqueous phosphate buffer (pH=7) in the presence of 0.1 mM KCl (Fig. 4c). The electrochemical platform exhibits a linearity range between 25 ng/mL and 200 ng/mL, with a Limit of Detection (LoD) of 5 ng/mL (SD = 0.2 for n=10) (Fig. 4d). Even if these results are promising, higher-sensitivity is required to reach advanced precision, moving closer to microgram per liters threshold and below (Union (2020)) .

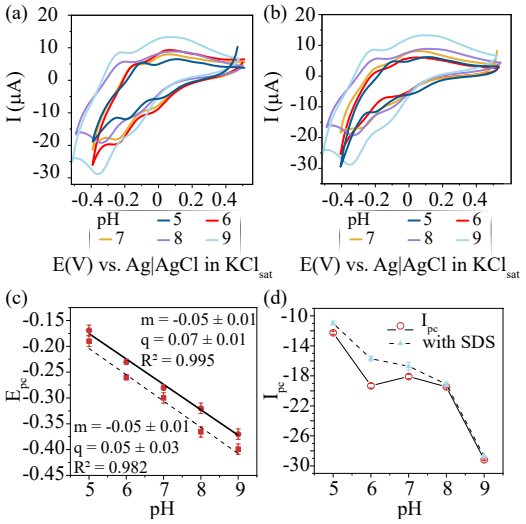

Figure 3: Cyclic voltammogramms (CVs) of p-MB/DRP110CNT recorded at pH 5-9 in the absence (a) and presence (b) of SDS 100 ng/mL at a scan rate of 50 mV/s. (c) Cathodic peak potential (E_{pc}) in the absence (dotted line) and presence (solid line) of SDS at 50 mV/s as a function of pH. (d) Cathodic peak current (I_{pc}) as a function of pH.

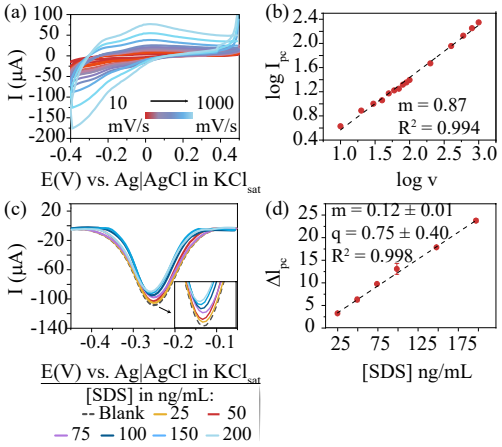

Figure 4: (a) Effect of increasing scan rate from 10 mV/s (in red) to 1000 mV/s (in light blue) in the presence of SDS (100 ng/mL) using p-MB/DRP110CNT; (b) double-log plot of log I_{pc} vs log v; (c) Square wave voltammetry (SWV) of p-MB/DRP110CNT with increasing SDS concentrations (25-200 ng/mL), and (d) calibration plot: ΔI_{pc} vs SDS concentration.

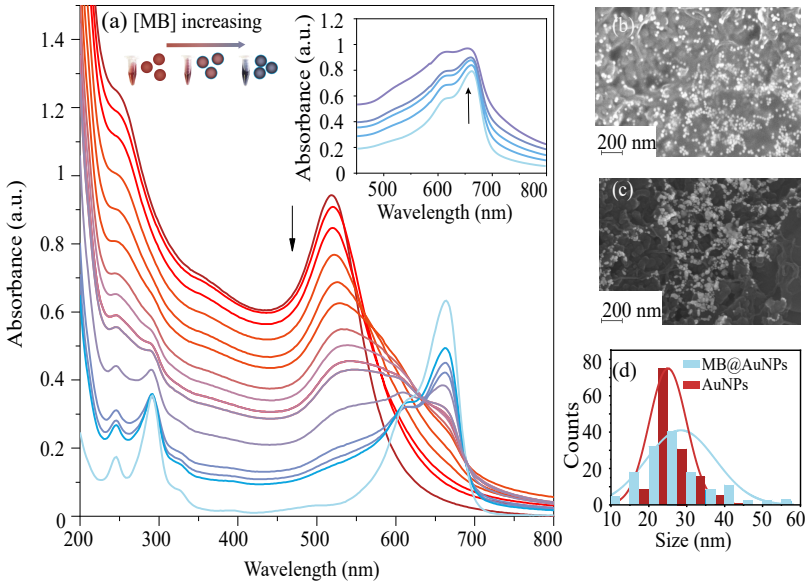

Figure 5: (a) Selected spectra during the titration of AuNPs with additions of 200 μL of MB (20 μM); each spectrum corresponds to one incremental addition of 200 μL, progressing from red (0 moles of MB added) to light blue (56 nmoli of MB added). Inset: selected spectra during the titration of MB (20 μM) in presence of different aliquots (200 μL) of AuNPs from light blue (0 moles of AuNPs added) to dark violet (2 pmoli of AuNPs added). In (b) and (c) SEM images of AuNPs and MB@AuNPs; (d) particle-size distribution (the diameter was measured by ImageJ software).

4.3. Preliminary Study of Opto-electrochemical Properties

To enhance the platform's sensitivity, the surface of the working electrode from the previous platform was modified with a layer-by-layer coating of gold nanoparticles (AuNPs) with a mean diameter of 25 nm (Fig. 5b), synthesized by the Turkevich citrate reduction method (Turkevich et al. (1951)). It was therefore conducted a preliminary study to evaluate the interactions between the thiazinic dye MB and the citrate-stabilized gold nanoparticles, as well as to investigate the mechanism of SDS interaction within this system. For this purpose, a fixed volume of gold nanoparticles was titrated with various aliquots of dye and the UV-Vis spectra were recorded, after system stabilization.

As observed in Fig. 5a following the additions of MB, the local plasmonic resonance of gold nanoparticles (LSPR) at 530 nm begins to decrease, and visually, the color of the nanoparticles starts to shift towards purple.

If no interaction had occurred, the band associated with LSPR would have decreased with increasing MB concentration, due to dilution effects, and a simple isosbestic peak would have been observed between the LSPR peak and the dye peak (Narband et al. (2009)). Conversely, after the addition of only 12 nmoles of MB, a small peak attributable to the dye begins to appear in the region between 600 and 700 nm of the spectrum. Continuing to add the dye, the LSPR peak begins to broaden due to nanoparticle precipitation, while the shoulder associated with MB becomes increasingly pronounced, until the LSPR peak disappears. As shown in the graph, there exists a threshold concentration above which the nanoparticles are completely coated with MB molecules and begin to precipitate. The found threshold concentration of MB from the UV-Vis spectrum is 0.32 μM (Shan et al. (2021)). Gold nanoparticles synthesized using the Turkevich method exhibit a weak negative charge, attributed to the citrate used as a stabilizer and reducing agent. Since the thiazine dye carries a positive charge, it interacts weakly with the gold nanoparticles. The high surface-to-volume ratio and ionic strength drive the adsorption of methylene blue molecules, which distribute around the nanoparticles, forming a Self-Assembled Monolayer (SAM) of dye. In literature (Narband et al. (2009)), it has been demonstrated that when a solution of cationic thiazinic dye, such as methylene blue or toluidine blue, is titrated with a gold colloid, the dye's extinction coefficient increases by up to ten fold. In the inset in Fig. 5a, it is possible to observe how the absorbance at 662 nm and 615 nm (in blue) increases with increasing concentration of added nanoparticles, reaching a maximum absorbance of 0.93 (at 662 nm), before starting to decrease. Already with the first addition of nanoparticles (200 μL), the extinction coefficient increases by approximately 30%, from $3.16 \cdot 10^4 Lmol^{-1}cm^{-1}$ to $4.03 \cdot 10^4 Lmol^{-1}cm^{-1}$ (at 662 nm). This increase is attributed to the coordination of thiazinic groups around the nanoparticle rather than nanoparticle aggregation (Ding et al. (2006)). As observed for thionine (Ding et al. (2006)), the packing of methylene blue molecules increases the local concentration of dye molecules, reflected in an increase in transversal absorption and thus absorption intensity of both the peak at 662 nm and the peak at 615 nm (Narband et al. (2009)). Additionally, the electronic coupling between adsorbed dye molecules on the nanoparticle causes a slight blue shift of the 662 nm band. The increase in intensity of the 615 nm peak associated with the dimer is instead may be attributed to the formation of clusters between nanoparticles, resulting from charge neutralization.The SEM images, shown in Fig. 5c, revealed the presence of those clusters. After

adding MB, the size of AuNPs slightly increases from 25 ± 0.3 nm to 29 ± 0.6 nm (Fig. 5d) and clusters of about 100 nm can be observed in Fig. 5c. To investigate the interaction between MB@AuNPs and the analytes, small aliquots of 1μL of aqueous solutions (to exclude dilution effects) of SDS and one long-chain PFAS, perfluorooctanesulfonic acid (PFOS), at concentrations ranging from 0.1 ng/ml to 5 ng/mL were added, and the UV-Vis spectrum was recorded each time (Fig. 6a-b).

As observed for a similar system (Grueso et al. (2023)), following additions of surfactant at a concentration very low respect to the CMC, the absorbance at 530 nm decreases, due to monomer interaction with NPs. Reporting the percentage absorbance change as a function of surfactant concentration (Fig. 6b) reveals a trend similar to an adsorption isotherm. Since the absorbance change $(A_0 - A_t)$ is proportional to the amount of surfactant absorbed, the data were fitted with various curves. Among these, the Sips model, described by the equation (Eq. 8):

$$\Theta = \frac{(KC)^n}{1 + (KC)^n} \tag{8}$$

where Θ is the fractional surface coverage, C is the surfactant concentration, K is the equilibrium constant, and n is the heterogeneity factor, provided the best fit. The *Sips* model is particularly suitable for describing surfactants adsorption on surfaces (Wang and Guo (2020)). This trend thus appears to confirm a potential adsorption of the SDS monomers around the functionalized gold nanoparticles. A very similar trend is also observed for PFOS (Fig. 6b); the values for the fitted K are 0.07 mL/ng and 0.05 mL/ng for SDS and PFOS respectively. Furthermore, the SERS spectra of AuNPs and MB@AuNPs have been acquired in the absence and presence of SDS in the spectral range between 200 and 2000 cm^{-1} (Fig. 6c-d). As observed for a similar system (Liang et al. (2017)), the addition of surfactant clearly diminishes the intensity of the SERS spectra. In particular, the main peaks associated with the dye at 440, 496 and 598 (C-N-C and C-S-C skeletal deformation) (Li et al. (2016)), at 663 and 704 (out-of-plan bending of C-H) (Li et al. (2016)), 880, 940, 1059, 1147 ((in-plan bending C-H) (Li et al. (2016)), and 1173 (stretching C-N) (Li et al. (2016)) undergo a significant and reproducible decrease in SERS intensity, suggesting the interaction with both the amino group and the planar rings of MB. To get additional insight into the interactions between MB and the surfactant, we have conducted a QM study of the MB-DS cluster by optimizing its structure using DFT cal-

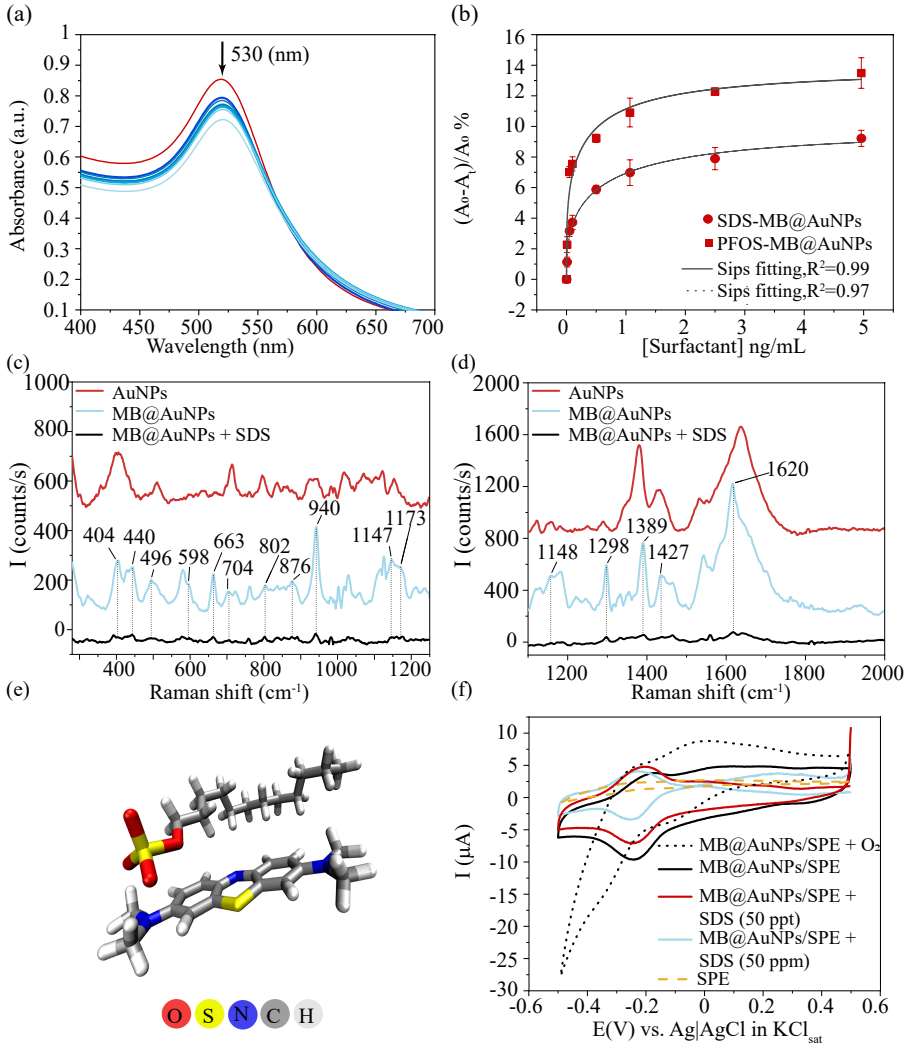

Figure 6: (a) UV-vis spectra of AuNPs after sequential additions of 1μL of PFOS solution. (b) Relative absorbance ($\Delta A/A_0$) as a function of surfactant concentration (ng/mL). The spectra range in color from dark blue to light blue with increasing PFOS concentration; the initial red spectrum corresponds to AuNPs in the absence of PFOS. In (c) and (d) SERS spectra (7-point *Savitzky-Golay* smoothing) of AuNPs (in red), of MB@AuNPs (in light blue), and of MB@AuNPs in the presence of SDS (black).(e) Optimized geometry of the methylene blue-dodecyl sulfate cluster. Carbon, hydrogen, nitrogen, sulfur, and oxygen atoms are shown in grey, white, blue, yellow, and red, respectively. (e) Cyclic voltammograms of MB immobilized on AuNPs/DRP110CNT: in the presence of O_2 (dotted black line), in the absence of O_2 (solid black line), with SDS at 50 pg/mL (solid red line) and 50 ng/mL (solid blue line), and on bare SPE (dashed yellow line).

culations. The optimized geometry is shown in Fig. 6e. As it can be seen, the MB cation and SDS anion form electrostatic interactions between one of the two $N^+(CH_3)_2$ group of MB which is positively charged and prefers to cluster with the anionic head group of SDS (SO_4^{2-}). Note that the optimized S-N distance is 3.63Å and the minimum optimized O-H distances are 2.02 and 2.28Å. Besides such electrostatic interactions, MB and SD also form hydrophobic interactions. The alkyl chain of the surfactant indeed arrange near the hydrophobic center of the dye, thus interacting via hydrophobic interactions with the MB planar rings. In order to quantify the strength of the interactions formed, we have calculated the interaction energy between MB and SD in the optimized structure which is of -14.5 kcal/mol. The results of the quantum mechanical calculation reveal the strong interaction between SDS and methylene blue through dispersive and electrostatic forces. Through these interactions, the surfactant can be adsorbed onto the surface of the electrode modified with methylene blue, altering the electronic and optical properties of the dye.

4.4. Electrochemical characterization and evaluation of the electroanalytical capability of the platform

After evaluating various fabrication methods, we selected post-deposition functionalization by directly drop-casting MB onto AuNPs-modified working electrode (WE), using a dye-to-nanoparticles ratio of 1:4, that was found optimal in preliminary studies. This modification technique proves advantageous, as it enhances both platforms sensitivity and processing efficiency (Wieszczycka et al. (2021)). CVs confirmed that MB binds irreversibly to AuNPs while retaining its electrochemical activity, contrary to some literature reports (Svetlii et al. (1993)). Specifically, as shown in Fig. 6f, MB exhibits reversible redox behavior with a ΔE of 50 mV (Ding et al. (2006)). In contrast, some literature studies, such as that by V. Svetlii et al. (Svetlii et al. (1993)), suggest that once MB is immobilized on a gold electrode, it loses its electrochemical activity. We also observed this phenomenon for pMB onto AuNPs-modified SPE (Fig. S7). SERS spectroscopy confirmed the interaction between SDS and MB, with SDS significantly damping MBs SERS signals (Fig. S5). Increasing SDS concentrations shifted MBs reduction peak to more negative potentials, indicating increased surface hydrophobicity and negative charge (Fig. 7a). The platform showed two linear response ranges for SDS detection (0.05 - 1 ng/mL and 5 - 50 ng/mL), with LoD values of 8.5 pg/mL and 0.23 ng/mL (Fig. 7b-c). The

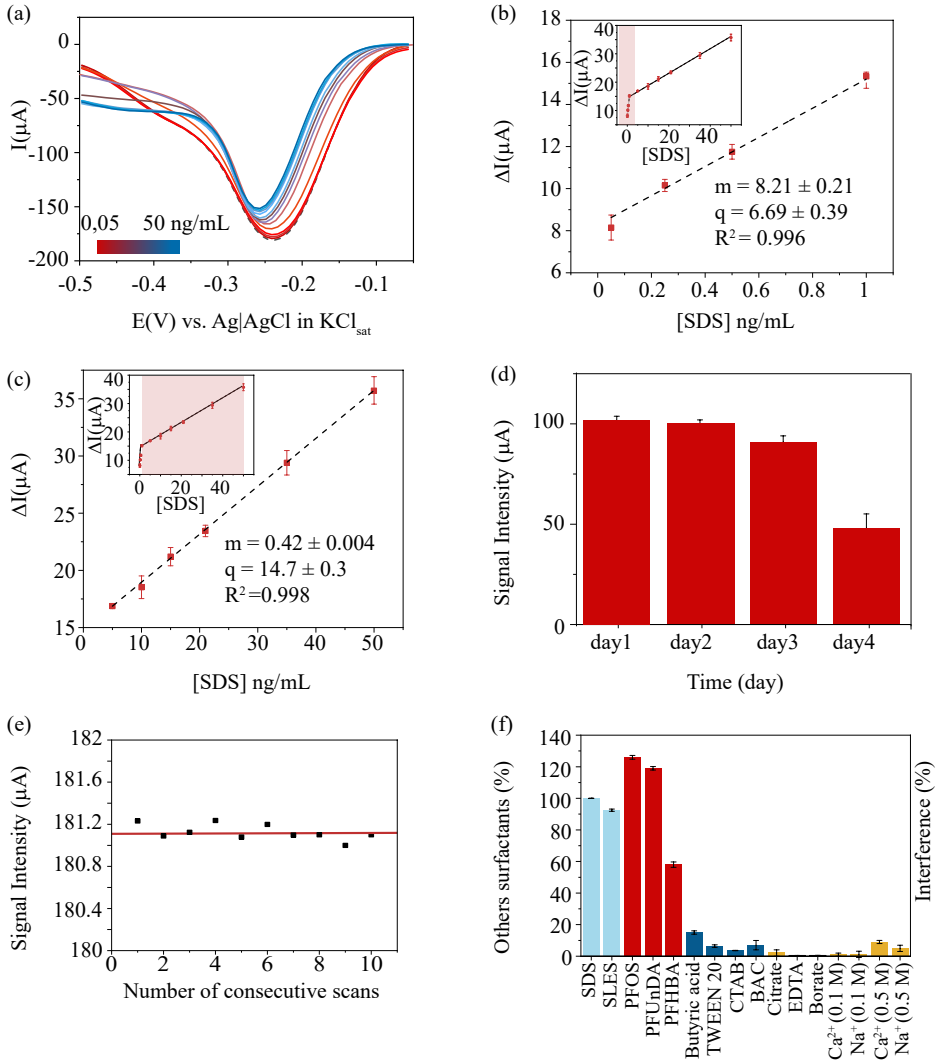

Figure 7: (a) Square wave voltammograms (SWVs) of MB@AuNPs/DRP110CNT in the presence of SDS (0.05-50 ng/mL, from red to dark blue); (b) Calibration curve for SDS in PBS (pH 7.0, 0.1 mM KCl), covering the range 0.051 ng/mL and (c) calibration curve covering the range 550 ng/mL. Insets show the full concentration interval, with the two linear response regions highlighted in pink for clarity; (d) Time stability. Error bars represent standard deviations (n=3); (e) Reproducibility and (f) selectivity evaluated using the anionic SLES (in light blue), PFHBA, PFOS, and PFunDA (25 ng/mL ea) (in red), butyric acid, TWEEN20, CTAB, BAC (25 ng/mL ea) (in blue) along with interference resistance (in yellow). Error bars represent standard deviations (n=7).

double linear trend is attributed to complex surfactant adsorption phenomena, which are related to the saturation of adsorption sites and/or onset micellization, that reduces SDS molecules availability (Hu and Bard (1997)). Sensor showed stable response during repeatable use: reproducibility was confirmed with ten successive SWVs in PBS, showing negligible signal variation (RSD=0.07%)(Fig. 7e); minimal output change was observed after 3 days storage respect to fresh electrode. Furthermore, the matrix effect was calculated to be 16.5 0.7% (n=7) with high selectivity for AS and PFAS (Fig. 7f). Specifically, the selectivity of the sensor was assessed by evaluating its response to other commonly used surfactants, including the commercial cationic surfactants cetyltrimethylammonium bromide (CTAB) and benzalkonium chloride (BAC), as well as the zwitterionic surfactant TWEEN 20 each at a concentration of 25 ng/mL. These surfactants are widely employed in pharmaceutical, cosmetic, and personal care products. CTAB and BAC are primarily used as antimicrobial agents, disinfectants, and antiseptics, while TWEEN 20 is commonly applied as a non-ionic emulsifier, stabilizer, and solubilizing agent in formulations such as creams, vaccines, and drug delivery systems (Amaral et al. (2008); Zheng et al. (2020)). Due to their extensive usewhich became particularly prominent during the COVID-19 pandemicand their potential functional similarity to the target analytes, these compounds represent possible interferents in sensor performance. However, as shown in Fig. 7f, the presence of these organic compounds did not significantly affect the sensor's ability to detect the target analytes. The sensor exhibited negligible signal changes (less than 10 %) or no response upon their introduction into the test solution. As described in the Materials and Methods section, the sensors response to SDS (25 ng/mL) was evaluated in the presence of common inorganic ions found in water (Ca^{2+}, Na^{+}) at two concentrations (0.1 M and 0.5 M), as well as in the presence of three anions commonly used in pharmaceutical and personal care product formulations (EDTA, citrate, and borate) at a fixed concentration of 0.1 M as in Glumac et al. (2024), to simulate potential co-occurrence in environmental water samples. From Fig. 7f, it is clear that the platform demonstrates outstanding resistance to inorganic ions, maintaining a robust SDS signal even at higher salt concentrations (0.5 M), demonstrating its sensitivity toward structurally related congeners. The sensor also features prominently in the electrochemical sensing of another tested anionic surfactant, SLES, which exhibited a response comparable to that of SDS. This platform was successfully employed for the analysis of three municipal wastewater efflu-

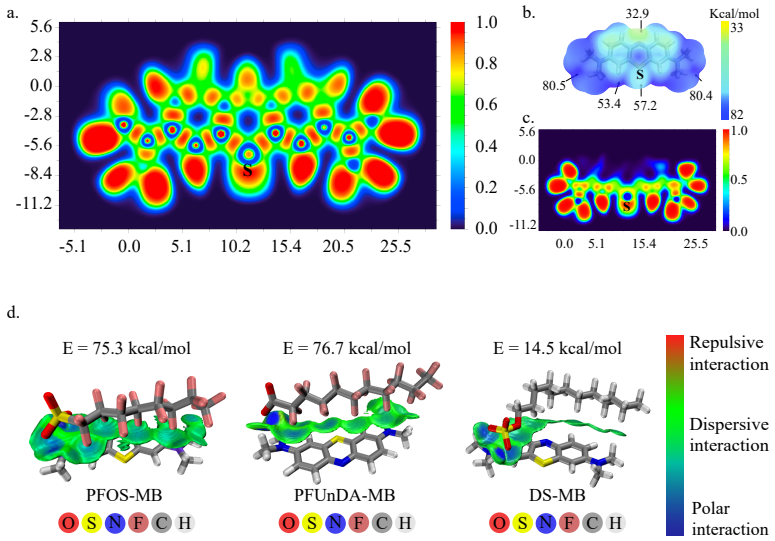

Figure 8: (a) Electron localization function (ELF) in Bohr and (b) molecular electrostatic potential (MEP) maps of MB; (c) ELF after PFOS adsorption; (d) IGMH analysis of PFOS-MB, PFnDA-MB, and DS-MB complexes.

ents, as reported in the SI. The results perfectly benchmark the reference MBAS method, with a relative error (E_r%) lower than 10%. Finally, the feasibility of using MB@AuNPs-modified SPE for the detection of PFAS was preliminary explored, including tests with one short-chain PFAS and two long-chain PFAS: perfluorobutanoic acid (PFHBA), perfluorooctanesulfonic acid (PFOS) and perfluoroundecanoic acid (PFUnDA). The proposed sensor exhibited a robust signal response for PFOS and PFUnDA, even higher than that of SDS (≈125 %) (Fig. 7f), suggesting its potential suitability for the detection of these pollutants. The sensor also demonstrated sensitivity to the tested short-chain PFAS, even if with a lower signal (≈58 %), yet still higher than that obtained for the aliphatic compound butyric acid (≈15 %), in agreement with the findings reported by Tang et al. (2025).

4.5. Promising PFAS detection in drinking water

Computational calculations were carried out to unveil the interaction mechanism between PFAS and MB, focusing on PFOS and PFUDA, which exhibited a higher response. To uncover the underlying electronic characteristics of MB, the electron localization function (ELF) of the dye was computed

using Multiwfn (Lu and Chen (2012)) and displayed in the color-filled map in Fig. 8a. Higher ELF values (>0.5), indicated in red, correspond to highly localized electrons, which suggest the presence of covalent bonds, inner shells, or lone electron pairs. In contrast, lower ELF values (<0.5) indicate regions of electron delocalization (Carpio-Martínez and Cortés-Guzmán (2023)). As shown in Fig. 8a, the color gradients confirm the occurrence of delocalized electrons, with maximum ELF values around hydrogen and sulfur atoms indicating the presence of bonding and non-bonding electrons (Karpagavalli et al. (2024)). Blue regions around the carbon atoms in aromatic rings reveal a de-localized electron cloud, while electron depletion regions between the valence and inner shells appear as small blue circles around carbon, sulfur, and nitrogen atoms. Additionally, the Molecular Electrostatic Potential (MEP) was calculated based on the optimized molecular configuration. The most positive regions in the map, shown in blue in Fig. 8b, represent electron-deficient areas primarily distributed around nitrogen atoms, which are the preferred adsorption sites for ASs (Shan et al. (2021)). The ELF color-filled map was computed after PFOS adsorption onto MB and displayed in Fig. 8c. As revealed by the map, PFOS cause a strong modification of ELF. Specifically, the interactions with PFOS modifies the map in the region of nitrogen atoms in the dimethylamino groups. Moreover, the modifications also involve the aromatic planar skeleton of MB, which becomes blue and partially disappeares from the map, suggesting a redistribution and a delocalization of the charge attributable to PFOS interaction.

PFAS-MB complexes, optimized at high theroretical level, are reported in Fig. 8d, and compared with DS-MB complex. Both PFOS-MB and PFUnDA-MB exhibited negative adsorption energies of -75.3 and -76.7 kcal/mol, respectively, with bond distances between 2.20 and 3.96 Å, suggesting the occurrence of strong interactions with the dye. The PFUnDA-MB complex exhibited a higher adsorption energy compared to the PFOS-MB complex, probably due to its longer chain length. Moreover, it is important to note that PFAS show stronger interaction energies with MB as compared with DS.

The nature of the interactions formed between the anion and the dye was further investigated through Hirshfeld partitioning of molecular density (IGMH) analysis (Lu and Chen (2022)). Blue and green zones mapped between fragments represent regions where attractive interactions occur that stabilize the complexes. As observable in Fig. 8d, in all the three complexes dispersive interactions are formed between the alkyl chain of the anion and

the MB aromatic skeleton. Aside from dispersion forces, IGMH analysis reveals the formation of electrostatic interactions, between one of the two positively charged dimethylamino groups of MB and the anionic head group.

An important aspect that is worth mentioning is that fluorines high electronegativity enables it to act as a Lewis base and to interact with positively charged MB forming stronger interactions as compared to hydrocarbon surfactants and contributing to increased adsorption energy (Leung et al. (2023)).

In light of these promising results, the platform was calibrated for the two previously tested PFAS under the optimized conditions found in the preliminary analyses and further confirmed (Fig. 9e-f and S8). Notably, it exhibited significantly higher sensitivity toward the tested PFAS compared to SDS, with a fivefold increase in sensitivity, fully aligned with computational predictions. As the concentration of PFAS increased, the peak current of MB decreased, indicating a linear relationship between peak current PFAS concentration, as for SDS. Regression parameters were evaluated to obtain insight into linearity. The coefficients of determination (R^2) for PFOS and PFUnDA were 0.998 and 0.999, respectively, demonstrating a nearly perfect linear fit. The calibration curves are shown in Fig. 9a-b, and the limits of detection (LoDs) were calculated to be 2.7 and 2.9 ppt for PFOS and PFUnDA, respectively.

To further validate its performance, SWV analysis was conducted on two fortified (0.2 ng/mL) tap water samples (Fig. 9e-f). As shown in Fig. 9e, sensor results closely match those obtained via the reference UHPLC-MS/MS method, achieving excellent recoveries for both long-chain sulfonic and carboxylic acids. Specifically, the sensors demonstrated recoveries ranging from 89% to 111%, for PFOS and PFUnDA respectively (Fig. 9e). Compared to conventional methods, the proposed platform exhibits outstanding accuracy and precision, with a maximum relative error (E_r%) of 11% in detecting PFOS and PFUnDA at ppt levels - a sensitivity achieved by only a few sensors reported in the literature (Tab. 1). Furthermore, the materials used for fabrication are cost-effective and easy to prepare, highlighting the potential of MB@AuNPs-based electrochemical sensors for detecting other PFAS congeners with suitable modifications.

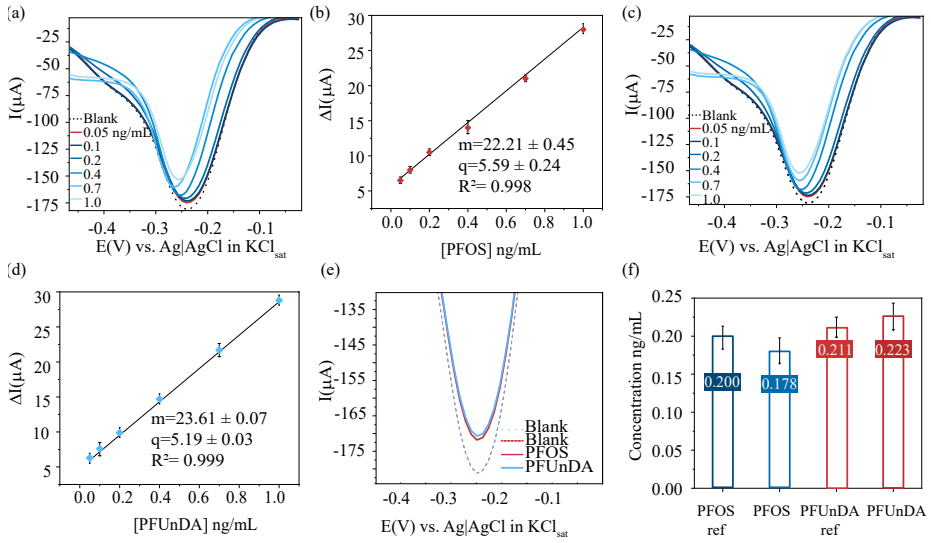

Figure 9: SWVs and linear calibration plots for PFOS (ab) and PFUnDA (cd) over the concentration range of 0.051 ng/mL; Error bars indicate the standard deviation (n = 7). (f) SWVs of spiked water samples and (e) comparison of the results with the reference method(n=3).

Table 1: Comparison of potential sensors for anionic surfactants and PFAS in water matrices

Platform	**Analytes**	**Range (μg/L)**	**LOD (μg/L)**	**Matrix**	**ref.**
MIP-Au SPE	PFOA	0.041-621.11	0.041	n.r.	Moro et al. (2021)
PVC-oNPOE-Au el.	PFCA-PFSA	0.5-5	0.025	n.r.	Garada et al. (2014b)
MIPs-Pencil lead el.	PFOA	4140.7-4140700.0	0.041	ww	Fang et al. (2016)
AgNPs on carbon fiber microel.	PFOS	0.010 - 1	0.037	n.r.	Khan et al. (2022)
o-PD MIP film + AuNS on GCE	PFOS	0.025 - 500	0.075	dw	Lu et al. (2022b)
o-PD MIP film on BDD/CNW el.	PFOS	0.1 - 100	1.2	dw and ww	Pierpaoli et al. (2023)
ZnONPs/MIP-SPE	SDS	288.3-2883	188	ww	Faradilla et al. (2021)
MB@AuNPs/DRP110CNT	SDS	0.05-1 and 5-50	0.0085 and 0.23	ww	This Work
MB@AuNPs/DRP110CNT	PFOS	0.05-1	0.0027	dw	This Work
MB@AuNPs/DRP110CNT	PFUnDA	0.05-1	0.0029	dw	This Work

Abbreviations: MIP Molecularly Imprinted Polymer; SPE Screen Printed Electrode; GCE Glassy Carbon electrode; PVC Poly Vinyl Chloride; oNPOE 2-Nitrophenyl Octyl Ether; CNWs B,N-codoped Carbon Nanowalls; PFCA Perfluoroalkyl Carboxylic Acid; PFSA Perfluoroalkyl Sulfonic Acid; ww wastewater; dw drinking water.

5. Conclusions

In conclusion, this research presents the fabrication of a novel electrochemical platform designed for the detection of anionic surfactants (ASs) at ppt and ppb concentration levels in aqueous matrices. Detection is facilitated by exploiting the selectivity and the redox properties of the MB dye, whose opto-electrochemical properties have been significantly enhanced by the intercalation of a AuNPs layer. This allows for the direct adsorption of the dye onto the working electrode (WE), thus reducing issues related to time, costs, and reproducibility. The interaction of SDS with the sensor was unveiled at a high chemical-physics level through optical and electrochemical techniques, revealing the selective interaction between the standard and the platform. This configuration shows excellent linear ranges: 0.051 ng/mL and 550 ng/mL, high reproducibility and sensibility (LoD of 8.5 pg/mL and 0.23 ng/mL), benchmarking the results of the reference MBAS method. In addition, the materials utilized to fabricate MB@AuNPs/DRP110CNT were both cost-effective and undemanding to prepare. Conclusively, the platform was tested and validated for PFOS and PFUnDA, yielding results consisting with that of the accredited method, and showing an even higher sensitivity, with a mechanism unveiled, for the first time, through computational calculations. While further studies are needed to fully validate its applicability and assess performance across a broader range of PFAS and environmental matrices, this platform offers promising prospects for both targeted and non-targeted electrochemical sensing of other PFAS congeners, with appropriate modifications, being potential as future early-warning tool supporting safe water management.

Declaration of competing interest

The authors declare that they have no known competing financial interests or personal relationships that could have appeared to influence the work reported in this paper.

Data availability

Data are not available.

Acknowledgements

The authors are grateful for the support of the National Center for Water Safety (CeNSIA) of the Italian National Institute of Health (ISS). This research was also made possible in part by ACEA Infrastructure S.p.A. for providing standards and materials. Finally, the authors wish to extend their thanks to Prof. Francesco Fatone and Prof. Anna Laura Eusebi of Marche Polytechnic University for their invaluable suggestions.

Supplementary materials

Supplementary materials associated with this article can be found in the online version.

Al Amin, M., Sobhani, Z., Liu, Y., Dharmaraja, R., Chadalavada, S., Naidu, R., Chalker, J.M., Fang, C., 2020. Recent advances in the analysis of per- and polyfluoroalkyl substances (pfas)a review. Environmental Technology & Innovation 19, 100879. doi:https://doi.org/10.1016/j.eti.2020.100879.

Amaral, M.H., das Neves, J., Oliveira, Â.Z., Bahia, M.F., 2008. Foamability of detergent solutions prepared with different types of surfactants and waters. Journal of surfactants and Detergents 11, 275–278.

Arora, J., Ranjan, A., Chauhan, A., Biswas, R., Rajput, V.D., Sushkova, S., Mandzhieva, S., Minkina, T., Jindal, T., 2022. Surfactant pollution, an emerging threat to ecosystem: Approaches for effective bacterial degradation. Journal of Applied Microbiology 133, 1229–1244. doi:https://doi.org/10.1111/jam.15631.

Badmus, S.O., Amusa, H.K., Oyehan, T.A., Saleh, T.A., 2021. Environmental risks and toxicity of surfactants: overview of analysis, assessment, and remediation techniques. Environmental Science and Pollution Research , 1–20doi:https://doi.org/10.1007/s11356-021-16483-w.

Barber, J.L., Berger, U., Chaemfa, C., Huber, S., Jahnke, A., Temme, C., Jones, K.C., 2007. Analysis of per-and polyfluorinated alkyl substances in air samples from northwest europe. Journal of environmental monitoring 9, 530–541. doi:https://doi.org/10.1039/b701417a.

Barone, V., Cossi, M., 1998. Quantum calculation of molecular energies and energy gradients in solution by a conductor solvent model. The Journal of Physical Chemistry A 102, 1995–2001. doi:https://doi.org/10.1039/B508541A.

Braun, W.A., Horn, B.C., Hoehne, L., Stlp, S., Rosa, M.B.D., Hilgemann, M., 2017. Poly(methylene blue)-modified electrode for indirect electrochemical sensing of oh radicals and radical scavengers. Anais da Academia Brasileira de Ciencias 89, 13811389. doi:https://doi.org/10.1590/0001-3765201720160833.

Cachet, C., Keddam, M., Mariotte, V., Wiart, R., 1993. Adsorption of perfluorinated surfactants on gold electrodesii. behaviour of ionic compounds. Electrochimica Acta 38, 2203–2208. doi:https://doi.org/10.1016/0013-4686(93)80099-L.

Canova, C., Barbieri, G., Jeddi, M.Z., Gion, M., Fabricio, A., Dapra, F., Russo, F., Fletcher, T., Pitter, G., 2020. Associations between perfluoroalkyl substances and lipid profile in a highly exposed young adult population in the veneto region. Environment International 145, 106117. doi:https://doi.org/10.1016/j.envint.2020.106117.

Cara, B., Lies, T., Thimo, G., Robin, L., Lieven, B., 2022. Bioaccumulation and trophic transfer of perfluorinated alkyl substances (pfas) in marine biota from the belgian north sea: Distribution and human health risk implications. Environmental Pollution 311, 119907. doi:https://doi.org/10.1016/j.envpol.2022.119907.

Carpio-Martínez, P., Cortés-Guzmán, F., 2023. Structural and bond evolutions during a chemical reaction, in: Advances in Quantum Chemical Topology Beyond QTAIM. Elsevier, pp. 53–71.

Carroll, M.K., Unger, M.A., Leach, A.M., Morris, M.J., Ingersoll, C.M., Bright, F.V., 1999. Interactions between methylene blue and sodium dodecyl sulfate in aqueous solution studied by molecular spectroscopy. Applied spectroscopy 53, 780–784. doi:https://doi.org/10.1366/0003702991947568.

Chen, X., Qadeer, A., Liu, M., Deng, L., Zhou, P., Mwizerwa, I.T., Liu, S., Ajmal, Z., Xingru, Z., Jiang, X., 2023. Chapter 13 - bioaccumulation of emerging contaminants in aquatic biota: Pfas as a case study,

in: Kumar, M., Mohapatra, S., Weber, K. (Eds.), Emerging Aquatic Contaminants. Elsevier, pp. 347–374. doi:https://doi.org/10.1016/B978-0-323-96002-1.00010-9.

Cheng, F., Yue-lin, L., Xing-yao, Z., 2001. The electrochemical properties of thionine adsorbed monolayer on gold electrode. Wuhan University Journal of Natural Sciences 6, 846–850. doi:https://doi.org/10.1007/BF02850916.

Cserhti, T., Forgcs, E., Oros, G., 2002. Biological activity and environmental impact of anionic surfactants. Environment International 28, 337–348. doi:https://doi.org/10.1016/S0160-4120(02)00032-6.

D'Ambro, E.L., Murphy, B.N., Bash, J.O., Gilliam, R.C., Pye, H.O., 2020. Predictions of pfas regional-scale atmospheric deposition and ambient air exposure. Science of The Total Environment 902, 166256. doi:https://doi.org/10.1016/j.scitotenv.2023.166256.

Deep, S., Ahluwalia, J.C., 2001. Interaction of bovine serum albumin with anionic surfactants. Physical Chemistry Chemical Physics 3, 4583–4591. doi:https://doi.org/10.1039/B105779K.

Ding, Y., Zhang, X., Liu, X., Guo, R., 2006. Adsorption characteristics of thionine on gold nanoparticles. Langmuir 22, 2292–2298. doi:https://doi.org/10.1021/la052897p.

Domingo, J.L., Nadal, M., 2019. Human exposure to per-and polyfluoroalkyl substances (pfas) through drinking water: A review of the recent scientific literature. Environmental research 177, 108648. doi:https://doi.org/10.1016/j.envres.2019.108648.

Fang, C., Megharaj, M., Naidu, R., 2016. Surface-enhanced raman scattering (sers) detection of fluorosurfactants in firefighting foams. RSC advances 6, 11140–11145. doi:https://doi.org/10.1039/C5RA26114G.

Fang, C., Zhang, X., Dong, Z., Wang, L., Megharaj, M., Naidu, R., 2018. Smartphone app-based/portable sensor for the detection of fluoro-surfactant pfoa. Chemosphere 191, 381–388. doi:https://doi.org/10.1016/j.chemosphere.2017.10.057.

Faradilla, P., Setiyanto, H., Manurung, R., Saraswaty, V., 2021. Electrochemical sensor based on screen printed carbon electrode - znonps/molecularly imprinted-polymer (spce-znonps/mip) for detection of sodium dodecyl sulfate (sds). RSC Advances 12, 743–752. doi:https://doi.org/10.1039/D1RA06862H.

Fenton, S.E., Ducatman, A., Boobis, A., DeWitt, J.C., Lau, C., Ng, C., Smith, J.S., Roberts, S.M., 2021. Per-and polyfluoroalkyl substance toxicity and human health review: Current state of knowledge and strategies for informing future research. Environmental toxicology and chemistry 40, 606–630. doi:https://doi.org/10.1002/etc.4890.

Gao, Y., Gou, W., Zeng, W., Chen, W., Jiang, J., Lu, J., 2023. Determination of perfluorooctanesulfonic acid in water by polydopamine molecularly imprinted/gold nanoparticles sensor. Microchemical Journal 187, 108378.

Garada, M.B., Kabagambe, B., Kim, Y., Amemiya, S., 2014a. Ion-transfer voltammetry of perfluoroalkanesulfonates and perfluoroalkanecarboxylates: picomolar detection limit and high lipophilicity. Analytical chemistry 86, 11230–11237.

Garada, M.B., Kabagambe, B., Kim, Y., Amemiya, S., 2014b. Ion-transfer voltammetry of perfluoroalkanesulfonates and perfluoroalkanecarboxylates: Picomolar detection limit and high lipophilicity. Analytical Chemistry 86, 11230–11237. doi:10.1021/ac5027836.

George, A.L., White, G.F., 1999. Optimization of the methylene blue assay for anionic surfactants added to estuarine and marine water. Environmental toxicology and chemistry 18, 2232–2236.

Germani, R., Bini, M., Fantacci, S., Simonetti, F., Tiecco, M., Vaioli, E., 2021. Influence of surfactants in improving degradation of polluting dyes photocatalyzed by tio2 in aqueous dispersion. Journal of Photochemistry and Photobiology A: Chemistry 418, 113342. doi:https://doi.org/10.1016/j.jphotochem.2021.113342.

Glumac, N., Momčilović, M., Kramberger, I., Štraus, D., Sakač, N., Kovač-Andrić, E., Jurin, B., Kraševac Sakač, M., Jambić, K., Jozanović, M., 2024. Potentiometric surfactant sensor with a pt-doped acid-activated

multi-walled carbon nanotube-based ionophore nanocomposite. Sensors 24, 2388.

Gomez, V., Ferreres, L., Pocurull, E., Borrull, F., 2011. Determination of non-ionic and anionic surfactants in environmental water matrices. Talanta 84, 859–866. doi:https://doi.org/10.1016/j.talanta.2011.02.009.

González-López, A., Costa-Rama, E., Fernández-Abedul, M.T., 2021. Electrochemical micropipette-tip for low-cost environmental applications: Determination of anionic surfactants through their interaction with methylene blue. Talanta 224, 121732. doi:https://doi.org/10.1016/j.talanta.2020.121732.

Grimme, S., Ehrlich, S., Goerigk, L., 2011. Effect of the damping function in dispersion corrected density functional theory. Journal of computational chemistry 32, 1456–65. doi:https://doi.org/10.1002/jcc.21759.

Grueso, E., Girldez-Prez, R.M., Prado-Gotor, R., Kuliszewska, E., 2023. Sodium lauryl sulfate-conjugated cationic gemini-surfactant-capped gold nanoparticles as model system for biomolecule recognition. Chemosensors 11. doi:https://doi.org/10.3390/chemosensors11040207.

Hu, K., Bard, A.J., 1997. Characterization of adsorption of sodium dodecyl sulfate on charge-regulated substrates by atomic force microscopy force measurements. Langmuir 13, 5418–5425. doi:10.1021/la970483t.

Humphrey, W., Dalke, A., Schulten, K., 1996. Vmd: visual molecular dynamics. Journal of molecular graphics 14, 33–38.

Iqbal, S., Ghafoor, A., Ayub, N., 2005. Relationship between sds-page markers and ascochyta blight in chickpea. Pakistan Journal of Botany 37, 87–96.

Junqueira, H.C., Severino, D., Dias, L.G., Gugliotti, M.S., Baptista, M.S., 2002. Modulation of methylene blue photochemical properties based on adsorption at aqueous micelle interfaces. Phys. Chem. Chem. Phys. 4, 2320–2328. doi:DOI https://doi.org/10.1039/B109753A.

Jurado, E., Fernández-Serrano, M., Nunez-Olea, J., Luzón, G., Lechuga, M., 2006. Simplified spectrophotometric method using methylene blue for determining anionic surfactants: applications to the study of primary biodegradation in aerobic screening tests. Chemosphere 65, 278–285.

Karpagavalli, K., Magdaline, J., Chithambarathanu, T., Vijaya, P., Amjesh, R., 2024. Quantum chemical evaluation, elf, lol analysis, fukui, herbicide-likeness and molecular docking studies of 4-methyl-phenoxyacetic acid, 4-acetyl-phenoxyacetic acid and 4-tert-butyl-phenoxyacetic acid-a comparative study. STRUCTURAL CHEMISTRY 35, 1307–1333.

Keller, S., Heerklotz, H., Jahnke, N., Blume, A., 2006. Thermodynamics of lipid membrane solubilization by sodium dodecyl sulfate. Biophysical journal 90, 4509–4521. doi:https://doi.org/10.1529/biophysj.105.077867.

Khan, R., Andreescu, D., Hassan, M.H., Ye, J., Andreescu, S., 2022. Nanoelectrochemistry reveals selective interactions of perfluoroalkyl substances (pfass) with silver nanoparticles. Angewandte Chemie 134, e202209164.

Khan, S., Alam, F., Azam, A., Khan, A.U., 2012. Gold nanoparticles enhance methylene blue–induced photodynamic therapy: a novel therapeutic approach to inhibit candida albicans biofilm. International journal of nanomedicine , 3245–3257doi:https://doi.org/10.2147/IJN.S31219.

Kim, S.K., Kannan, K., 2007. Perfluorinated acids in air, rain, snow, surface runoff, and lakes: relative importance of pathways to contamination of urban lakes. Environmental science & technology 41, 8328–8334. doi:10.1021/es072107t.

Kovalchuk, N., Trybala, A., Starov, V., Matar, O., Ivanova, N., 2014. Fluoro-vs hydrocarbon surfactants: why do they differ in wetting performance? Advances in colloid and interface science 210, 65–71. doi:https://doi.org/10.1016/j.cis.2014.04.003.

Kurwadkar, S., Dane, J., Kanel, S.R., Nadagouda, M.N., Cawdrey, R.W., Ambade, B., Struckhoff, G.C., Wilkin, R., 2022. Per-and polyfluoroalkyl substances in water and wastewater: A critical review of their global occurrence and distribution. Science of The Total Environment 809, 151003. doi:https://doi.org/10.1016/j.scitotenv.2021.151003.

Lada, Z.G., Mathioudakis, G.N., Beobide, A.S., Andrikopoulos, K.S., Voyiatzis, G.A., 2024. Generic method for the detection of short & long chain pfas extended to the lowest concentration levels of sers capability. Chemosphere 363, 142916.

Lamichhane, H.B., Arrigan, D.W., 2023. Electroanalytical chemistry of per- and polyfluoroalkyl substances. Current Opinion in Electrochemistry 40, 101309.

Laviron, E., 1979. General expression of the linear potential sweep voltammogram in the case of diffusionless electrochemical systems. Journal of Electroanalytical Chemistry and Interfacial Electrochemistry 101, 19–28. doi:https://doi.org/10.1016/S0022-0728(79)80075-3.

Leung, S.C.E., Wanninayake, D., Chen, D., Nguyen, N.T., Li, Q., 2023. Physicochemical properties and interactions of perfluoroalkyl substances (pfas)-challenges and opportunities in sensing and remediation. Science of The Total Environment 905, 166764.

Li, C., Huang, Y., Lai, K., Rasco, B.A., Fan, Y., 2016. Analysis of trace methylene blue in fish muscles using ultra-sensitive surface-enhanced raman spectroscopy. Food Control 65, 99–105. doi:https://doi.org/10.1016/j.foodcont.2016.01.017.

Liang, A., Wang, X., Wen, G., Jiang, Z., 2017. A sensitive and selective victoria blue 4r sers molecular probe for sodium lauryl sulfate in aunp/agcl sol substrate. Sensors and Actuators B: Chemical 244, 275–281. doi:https://doi.org/10.1016/j.snb.2016.12.151.

Lu, D., Zhu, D.Z., Gan, H., Yao, Z., Luo, J., Yu, S., Kurup, P., 2022a. An ultra-sensitive molecularly imprinted polymer (mip) and gold nanostars (auns) modified voltammetric sensor for facile detection of perfluorooctance sulfonate (pfos) in drinking water. Sensors and Actuators B: Chemical 352, 131055.

Lu, D., Zhu, D.Z., Gan, H., Yao, Z., Luo, J., Yu, S., Kurup, P., 2022b. An ultra-sensitive molecularly imprinted polymer (mip) and gold nanostars (auns) modified voltammetric sensor for facile detection of perfluorooctance sulfonate (pfos) in drinking water. Sensors and Actuators B: Chemical 352, 131055. URL: https://www.sciencedirect.com/science/article/pii/S0925400521016233, doi:https://doi.org/10.1016/j.snb.2021.131055.

Lu, T., Chen, F., 2012. Multiwfn: A multifunctional wavefunction analyzer. Journal of computational chemistry 33, 580–592.

Lu, T., Chen, Q., 2022. Independent gradient model based on hirshfeld partition: A new method for visual study of interactions in chemical systems. Journal of computational chemistry 43, 539–555.

Mancini, M., Gioia, V., Simonetti, F., Frugis, A., Cinti, S., 2023. Evaluation of pure pfas decrease in controlled settings. ACS Measurement Science Au 3, 444–451. doi:10.1021/acsmeasuresciau.3c00027.

Marinho, M.I.C., Cabral, M.F., Mazo, L.H., 2012. Is the poly (methylene blue)-modified glassy carbon electrode an adequate electrode for the simple detection of thiols and amino acid-based molecules? Journal of Electroanalytical Chemistry 685, 8–14. doi:https://doi.org/10.1016/j.jelechem.2012.08.023.

Menger, R.F., Funk, E., Henry, C.S., Borch, T., 2021. Sensors for detecting per-and polyfluoroalkyl substances (pfas): A critical review of development challenges, current sensors, and commercialization obstacles. Chemical Engineering Journal 417, 129133. doi:https://doi.org/10.1016/j.cej.2021.129133.

Möller, A., Ahrens, L., Surm, R., Westerveld, J., van der Wielen, F., Ebinghaus, R., de Voogt, P., 2010. Distribution and sources of polyfluoroalkyl substances (pfas) in the river rhine watershed. Environmental Pollution 158, 3243–3250. doi:https://doi.org/10.1016/j.envpol.2010.07.019.

Moro, G., Chiavaioli, F., Liberi, S., Zubiate, P., Del Villar, I., Angelini, A., De Wael, K., Baldini, F., Moretto, L.M., Giannetti, A., 2021. (invited)nanocoated fiber label-free biosensing for perfluorooctanoic acid detection by lossy mode resonance. Results in Optics 5, 100123. doi:https://doi.org/10.1016/j.rio.2021.100123.

Muthaiyan Ahalliya, R., Daniel Raja, F.S., Rangasamy, K., Arumugam, V., Palanisamy, S., Saikia, K., Rathankumar, A.K., Al-Dhabi, N.A., Arasu, M.V., 2023. Production Cost of Traditional Surfactants and Biosurfactants. Springer Nature Switzerland, Cham. pp. 495–511.

Nakama, Y., 2017. Surfactants. Cosmetic science and technology: theoretical principles and applications 1, 231–244. doi:https://doi.org/10.1016/B978-0-12-802005-0.00015-X.

Narband, N., Uppal, M., Dunnill, C.W., Hyett, G., Wilson, M., Parkin, I.P., 2009. The interaction between gold nanoparticles and cationic and anionic dyes: enhanced uv-visible absorption. Physical Chemistry Chemical Physics 11, 10513–10518. doi:https://doi.org/10.1039/B909714G.

Neese, F., 2012. The orca program system. WIRES Comput. Molec. Sci. 2, 73–78. doi:10.1002/wcms.81.

Panieri, E., Baralic, K., Djukic-Cosic, D., Buha Djordjevic, A., Saso, L., 2022. Pfas molecules: a major concern for the human health and the environment. Toxics 10, 44. doi:https://doi.org/10.3390/toxics10020044.

Perdew, J.P., Burke, K., Ernzerhof, M., 1996. Generalized gradient approximation made simple. Phys. Rev. Lett. 77, 3865–3868. doi:10.1103/PhysRevLett.77.3865.

Pereira, L.C., de Souza, A.O., Bernardes, M.F.F., Pazin, M., Tasso, M.J., Pereira, P.H., Dorta, D.J., 2015. A perspective on the potential risks of emerging contaminants to human and environmental health. Environmental Science and Pollution Research 22, 13800–13823.

Pfaffen, V., Ortiz, P., Crdoba de Torresi, S., Torresi, R., 2010. On the ph dependence of electroactivity of poly(methylene blue) films. Electrochimica Acta 55, 1766–1771. doi:https://doi.org/10.1016/j.electacta.2009.10.062.

Pierpaoli, M., Szopińska, M., Olejnik, A., Ryl, J., Fudala-Ksiażek, S., Łuczkiewicz, A., Bogdanowicz, R., 2023. Engineering boron and nitrogen codoped carbon nanoarchitectures to tailor molecularly imprinted polymers for pfos determination. Journal of Hazardous Materials 458, 131873.

Podder, A., Sadmani, A.A., Reinhart, D., Chang, N.B., Goel, R., 2021. Per and poly-fluoroalkyl substances (pfas) as a contaminant of emerging concern in surface water: A transboundary review of their occurrences and toxicity effects. Journal of Hazardous Materials 419, 126361. doi:https://doi.org/10.1016/j.jhazmat.2021.126361.

Polli, F., Simonetti, F., Surace, L., Agostini, M., Favero, G., Mazzei, F., Zumpano, R., 2023. Nanoparticles in electrochemical immunosensors–a concept and perspective. ChemElectroChem , e202300408doi:https://doi.org/10.1002/celc.202300408.

Poothong, S., Thomsen, C., Padilla-Sanchez, J.A., Papadopoulou, E., Haug, L.S., 2017. Distribution of novel and well-known poly-and perfluoroalkyl substances (pfass) in human serum, plasma, and whole blood. Environmental science & technology 51, 13388–13396. doi:10.1021/acs.est.7b03299.

Prieto, G., Del Rio, J., Andrade, M.P., Sarmiento, F., Jones, M., 1993. Interaction between sodium n-undecyl sulfate and insulin. International journal of biological macromolecules 15, 343–345. doi:https://doi.org/10.1016/0141-8130(93)90051-M.

Ranaweera, R., An, S., Cao, Y., Luo, L., 2023. Highly efficient preconcentration using anodically generated shrinking gas bubbles for per-and polyfluoroalkyl substances (pfas) detection. Analytical and Bioanalytical Chemistry 415, 4153–4162.

Rehman, A.U., Locke, E., Andreescu, S., 2025. Spectroelectrochemical investigation of the interaction of perfluorooctane sulfonic acid (pfos) with organic dyes. Microchemical Journal 209, 112683.

Ródenas-Torralba, E., Reis, B.F., Morales-Rubio, Á., de la Guardia, M., 2005. An environmentally friendly multicommutated alternative to the reference method for anionic surfactant determination in water. Talanta 66, 591–599. doi:https://doi.org/10.1016/j.talanta.2004.12.006.

Sahu, S.P., Kole, S., Arges, C.G., Gartia, M.R., 2022. Rapid and direct perfluorooctanoic acid sensing with selective ionomer coatings on screen-printed electrodes under environmentally relevant concentrations. ACS omega 7, 5001–5007.

Sen, P.K., Mukherjee, P., Pal, B., 2016. Effects of pre-micelles of anionic surfactant sds on the electron transfer reaction between methylene blue and ascorbic acid. Journal of Molecular Liquids 224, 472–479. doi:https://doi.org/10.1016/0022-0728(93)80052-J.

Shan, F., Panariello, L., Wu, G., Gavriilidis, A., Fielding, H.H., Parkin, I.P., 2021. A study of the interaction of cationic dyes with gold nanostructures. RSC advances 11, 17694–17703. doi:https://doi.org/10.1039/D1RA03459F.

Shyichuk, A., Ziółkowska, D., 2016. Determination of anionic surfactants by means of photometric titration with methylene blue dye. Journal of Surfactants and Detergents 19, 425–429. doi:https://doi.org/10.1007/s11743-015-1779-2.

Simonetti, F., Brillarelli, S., Agostini, M., Mancini, M., Gioia, V., Murtas, S., Migliorati, V., 2025a. A review on the latest frontiers in water quality in the era of emerging contaminants: A focus on perfluoroalkyl compounds. Environmental Pollution , 126402URL: https://www.sciencedirect.com/science/article/pii/S0269749125007754, doi:https://doi.org/10.1016/j.envpol.2025.126402.

Simonetti, F., Mancini, M., Gioia, V., Zumpano, R., Mazzei, F., Frugis, A., Migliorati, V., 2025b. Unveiling the adsorption mechanism of perfluorooctane sulfonate onto polypropylene nanoplastics: A combined theoretical and experimental investigation. Water Research 278, 123324.

Simonetti, F., Polli, F., Di Costanzo, R., Nichele, L., Simonetti, G., Hwang, J.Y., Agostini, M., Mazzei, F., Zumpano, R., 2025c. Determination of the chemical oxygen demand using a cu-au anisotropic nanoalloy-modified screen-printed electrode: A sustainable and sensitive solution. ChemElectroChem , 2400610.

Sun, W., Wang, Y., Zhang, Y., Ju, X., Li, G., Sun, Z., 2012. Poly(methylene blue) functionalized graphene modified carbon ionic liquid electrode for the electrochemical detection of dopamine. Analytica Chimica Acta 751, 59–65. doi:https://doi.org/10.1016/j.aca.2012.09.006.

Svetlii, V., Clavilier, J., uti, V., Chevalet, J., Elachi, K., 1993. Effect of sulphur-adlayer preparation on self-assembled monolayers of phenothiazines at polyoriented platinum electrodes. Journal of Electroanalytical Chemistry 344, 145–160. doi:https://doi.org/10.1016/0022-0728(93)80052-J.

Taj Muhammad, M., Khan, M.N., 2017. Study of electrolytic effect on the interaction between anionic surfactant and methylene blue using spectrophotometric and conductivity methods. Journal of Molecular Liquids 234, 309–314. doi:https://doi.org/10.1016/j.molliq.2017.03.102.

Tang, X., Liu, G., Wang, D., Zhong, H., 2025. Methylene blue method for analysis of perfluoroalkyl substances (pfas): Effect of the molecular structure of pfas compounds. Journal of Hazardous Materials 492, 138187. URL: https://www.sciencedirect.com/science/article/pii/S0304389425011021, doi:https://doi.org/10.1016/j.jhazmat.2025.138187.

Tolls, J., Kloepper-Sams, P., Sijm, D.T., 1994. Surfactant bioconcentration-a critical review. Chemosphere 29, 693–717. doi:https://doi.org/10.1016/0045-6535(94)90040-x.

Turkevich, J., Stevenson, P.C., Hillier, J., 1951. A study of the nucleation and growth processes in the synthesis of colloidal gold. Discuss. Faraday Soc. 11, 55–75. doi:https://doi.org/10.1039/DF9511100055.

Union, E., 2020. Directive (eu) 2020/2184 of the european parliament and of the council of 16 december 2020 on the quality of water intended for human consumption. Official Journal of the European Union 435, 1–62.

Wang, J., Guo, X., 2020. Adsorption isotherm models: Classification, physical meaning, application and solving method. Chemosphere 258, 127279. doi:https://doi.org/10.1016/j.chemosphere.2020.127279.

Wang, Q., Tsui, M.M., Ruan, Y., Lin, H., Zhao, Z., Ku, J.P., Sun, H., Lam, P.K., 2019. Occurrence and distribution of per- and polyfluoroalkyl substances (pfass) in the seawater and sediment of the south china sea coastal region. Chemosphere 231, 468–477. doi:https://doi.org/10.1016/j.chemosphere.2019.05.162.

Weigend, F., Ahlrichs, R., 2005. Balanced basis sets of split valence, triple zeta valence and quadruple zeta valence quality for h to rn: Design and assessment of accuracy. Physical Chemistry Chemical Physics 7, 3297–3305.

Wieszczycka, K., Staszak, K., Woniak-Budych, M.J., Litowczenko, J., Maciejewska, B.M., Jurga, S., 2021. Surface functionalization the way for advanced applications of smart materials. Coordination Chemistry Reviews 436, 213846. URL: https://www.sciencedirect.com/science/article/pii/S0010854521000801, doi:https://doi.org/10.1016/j.ccr.2021.213846.

Wyrwas, B., Zgoła-Grześkowiak, A., 2014. Continuous flow methylene blue active substances method for the determination of anionic surfactants in river water and biodegradation test samples. Journal of Surfactants and Detergents 17, 191–198. doi:https://doi.org/10.1007/s11743-013-1469-x.

Yogeswaran, U., Chen, S.M., 2008. Multi-walled carbon nanotubes with poly(methylene blue) composite film for the enhancement and separation of electroanalytical responses of catecholamine and ascorbic acid. Sensors and Actuators B: Chemical 130, 739–749. doi:https://doi.org/10.1016/j.snb.2007.10.040.

Zheng, G., Filippelli, G.M., Salamova, A., 2020. Increased indoor exposure to commonly used disinfectants during the covid-19 pandemic. Environmental science & technology letters 7, 760–765.

Zumpano, R., Lambertini, L., Tortolini, C., Bollella, P., Favero, G., Antiochia, R., Mazzei, F., 2020. A glucose/oxygen enzymatic fuel cell exceeding 1.5v based on glucose dehydrogenase immobilized onto polymethylene blue-carbon nanotubes modified double-sided screen printed electrodes: Proof-of-concept in human serum and saliva. Journal of Power Sources 476, 228615. doi:https://doi.org/10.1016/j.jpowsour.2020.228615.